Title

Magnetite biomineralization in ferruginous waters and early Earth evolution

Authors

K. W. Bauer[1‡], J. M. Byrne[2], P. Kenward, R. L. Simister[1], C. C. Michiels[1], A. Friese[3], A. Vuillemin[3†], C. Henny[4], S. Nomosatryo[3,4], J. Kallmeyer[3], A. Kappler[2], M. A. Smit[1], R. Francois[1] and S. A. Crowe[1‡*]

Affiliations

[1]Departments of Microbiology and Immunology and Earth, Ocean and Atmospheric Sciences, The University of British Columbia, 2020 - 2207 Main Mall, Vancouver, British Columbia V6T 1Z4, Canada

[2]Center for Applied Geosciences, University of Tuebingen, 72076 Tuebingen, Germany

[3]GFZ German Research Centre for Geosciences, Helmholtz Centre Potsdam, 14473 Potsdam, Germany

[4] Research Center for Limnology, Indonesia Institute of Sciences (LIPI), Cibinong Science Centre, Cibinon-Bogor, Indonesia

[‡]Current Address: Department of Earth Sciences, University of Hong Kong, Pokfulam Road, Hong Kong SAR

[†]Current Address: Department of Earth and Environmental Sciences, Paleontology and Geobiology, Ludwig-Maximilians-Universität, Richard-Wagner-Str. 10, 80333 Munich, Germany

*Corresponding author; sean.crowe@ubc.ca

Abstract

Burial of large quantities of magnetite ($Fe(II)Fe(III)_2O_4$) in iron formations (IFs) likely contributed to the protracted oxidation of Earth's surface during the Precambrian Eons. Magnetite can form through a diversity of biological and abiotic pathways and its preservation in IFs may thus be variably interpreted as the result of some combination of these processes. Such interpretations thus give rise to divergent pictures of the Precambrian Earth system and models for its evolution through time. New knowledge on the contribution of specific magnetite formation pathways is, therefore, needed to accurately tether our conceptual and numerical models to the geologic record. To constrain pathways of magnetite formation under ferruginous conditions, we conducted geochemical and multi-method microspectroscopic analyses on particles obtained from the water columns and sediments of ferruginous lakes Matano and Towuti, in Indonesia. We find that biologically reactive Fe(III) mineral phases are entirely reduced in the anoxic waters of both lakes, leading to the formation of primary authigenic magnetite, directly in the water column. This water column magnetite often takes conspicuous framboidal forms, which given the link to microbial Fe(III) reduction, may provide a biological signature on early Earth and by extension, other planetary bodies. The consumption of more biologically reactive forms of Fe(III) and the resulting delivery of primary magnetite to underlying sediments controls sediment redox budgets and implies that primary magnetite formation could have been a principal mode of Fe delivery to IFs. Combined, the removal of Fe from Earth's surface through magnetite biomineralization and subsequent burial in IFs, suggests that seawater chemistry and the microbially mediated reactions that cause magnetite formation played key roles in Earth system evolution and in setting the pace for planetary oxidation through the Precambrian Eons.

Highlights

- Magnetite forms raspberry-like, framboidal grains through microbial iron reduction in the water column of two ferruginous lakes.
- Water column magnetite formation is a principal source of Fe to underlying sediments.
- The formation of water column magnetite exerts a primary control on sediment redox budgets.
- Water column magnetite formation likely contributed to IF deposition during the Precambrian Eons.

1.0 Introduction

Biogeochemical cycling of iron (Fe) and carbon (C) plays a key role in setting Earth's surface redox budgets and climate. Burial of reduced forms of C and Fe in marine sediments as organic matter (OM) and ferrous Fe (Fe(II))-bearing minerals, in particular, oxidize Earth's surface and represent quantitatively important net sources of oxygen to the modern atmosphere (Berner, 2003; Claire et al., 2006; Holland, 2006). Oxidation of crust-derived Fe(II) to form Fe(III)-bearing minerals, by contrast, is a net sink for atmospheric oxygen (Holland, 1984; Holland, 2002). The magnitudes of these sources and sinks are influenced by dynamics in coupled C and Fe cycling, which can induce secular variation in Earth's surface chemistry (Catling and Claire, 2005; Holland, 2002, 2006; Kasting, 2013) and over geological timescales this can lead to fundamentally different ocean-atmosphere redox states and climate systems (Holland, 2002; Kasting, 2013).

During much of the Precambrian Eons, the ocean-atmosphere system was nearly oxygen-free and rich in reduced chemical species (Fe(II), H_2 and CH_4) (Catling et al., 2001; Zerkle et al., 2012). Widespread deposition of Fe minerals at this time formed sedimentary iron formations (IFs) as the result of coupled C and Fe cycling in the oceans. Today these deposits contain vast quantities of both ferric [Fe(III)] and ferrous [Fe(II)] iron, the ratio of which can vary appreciably across IF facies leading to an overall mean iron redox state of 2.6 (Beukes and Klein, 1990; Klein, 2005). IF mineralogy, notably, is dominated by the mixed-valence oxide magnetite ($Fe^{2+}Fe^{3+}{}_2O_4$) (Klein, 2005), and burial of magnetite in IFs played an important role as a sink for Fe and in setting the redox state IFs with implications for evolution of the ocean-atmosphere system (Holland, 1984; Holland, 2002; Johnson et al., 2008; Walker, 1984). The oxidation of crustal Fe(II) to form Fe(III) buried as magnetite in IFs represented a net oxidant sink for the Earth's surface, which would have ultimately led to the production of H_2 as the corresponding sink for reduced equivalents (reaction 1);

$$3FeO + H_2O \rightarrow Fe_3O_4 + H_2 \qquad (1)$$

Such H_2 production promotes planetary oxidation when H_2 is lost to space (Holland, 2002; Kasting, 2013). The net effect of magnetite burial in IFs on Earth's global redox budget is represented by reaction (1) and is the same regardless of the pathway through which it forms. The factors controlling magnetite formation and burial in IFs and the ultimate production of

hydrogen, however, such as coupled C and Fe cycling directly in the oceans or diagenetic and metamorphic reactions, can be very different. This has important implications for interpretations of Precambrian seawater chemistry and biology, which we explore below.

The precise pathways for magnetite formation and ultimate burial in IFs remain poorly constrained and thus models that aim to mechanistically link the deposition of IFs to the evolution of Earth's surface redox budgets remain uncertain. The provenance of magnetite in IFs is contentious, but its formation is widely attributed to early diagenetic and or metamorphic reactions (Johnson et al., 2008; Konhauser et al., 2005; Walker, 1984). Magnetites contained in IFs exhibit low-grade metamorphic textures, implying recrystallization of primary IF mineral assemblages and the overprinting of original fabrics (Karlin et al., 1987; Klein, 2005; Li et al., 2013; Lovley, 1991). Many diagenetic and metamorphic models for magnetite formation suggest primary Fe deposition as Fe(III) (oxyhydr)oxides (ferrihydrite, goethite) (Halama et al., 2016; Klein, 2005) and mixed valence (oxyhydr)oxides (green rust) (Halevy et al., 2017; Koeksoy et al., 2019; Zegeye et al., 2012), with later-stage diagenetic (reaction 2) and thermochemical (reaction 3) reactions transforming these precursor phases to magnetite through reactions such as;

$$Fe^{2+} + 2Fe(OH)_3 + 2OH^- \rightarrow Fe_3O_4 + 4H_2O \qquad (2)$$

$$Fe_2O_3 + Fe^{2+} + H_2O \rightarrow Fe_3O_4 + 2H^+ \qquad (3)$$

Notably, magnetite formation via reactions (2) and (3) is not necessarily the direct product of coupled C and Fe cycling in the oceans. Thus magnetite formed in this way is decoupled from the physicochemical and biological conditions and processes in the ocean-atmosphere system at the time of magnetite formation and IF deposition. In contrast, precipitation and burial of primary magnetite in IFs would directly link IF mineralogy to the principal water column processes that cause IF deposition.

Precipitation of primary magnetite directly in the water column of the Precambrian oceans may also have been possible, as magnetite forms in laboratory experiments as the product of biological processes including magnetosome formation in magnetotactic bacteria (Amor et al., 2015), anoxygenic Fe(II) photosynthesis (Jiao et al., 2005) and Fe(III) respiration (Lovley, 1991; Lovley et al., 1987). These processes were all likely widespread under ferruginous ocean conditions (Halevy et al., 2017; Konhauser et al., 2005; Tosca et al., 2016; Zegeye et al., 2012).

Magnetite formation through these processes occurs through the reaction of seawater Fe(II) and Fe(III) (oxyhydr)oxides produced either through reaction with oxygen directly or through anoxygenic photosynthesis with Fe(II) as the electron donor (reactions 4 and 5);

$$4Fe^{2+} + HCO_3^- + 10H_2O \rightarrow CH_2O + 4Fe(OH)_3 + 7H^+ \quad (4)$$

$$Fe^{2+} + 2Fe(OH)_3 + 2OH^- \rightarrow Fe_3O_4 + 4H_2O \quad (5)$$

The extent to which such processes lead to magnetite formation depends on the concentration of Fe(II) in seawater, production rate of Fe(III) (oxyhydr)oxides, and other physicochemical parameters such pH, temperature and settling velocity, among others. The organic C produced via anoxygenic photosynthesis (reaction 4), furthermore, may also become consumed in anaerobic Fe(III) respiration (reaction 6) and fermentation (reaction 7) reactions that ultimately fuel competing Fe mineralization pathways;

$$CH_2O + 4Fe(OH)_3 + 8H^+ \rightarrow 4Fe^{2+} + 8HCO_3^- + 3H_2O \quad (6)$$

$$CH_2O + H_2O \rightarrow 2H_2 + CO_2 \quad (7)$$

For example, organic C not consumed by Fe(III) reduction may be channeled through fermentation (reaction 7), producing dissolved inorganic carbon species (DIC). High concentrations of DIC and Fe(II) in turn tend to favor the formation of the reduced Fe-carbonate mineral siderite over magnetite (Roh et al., 2003; Vuillemin et al., 2019). The organic C consumed via reaction (7), furthermore, is not buried and also produces an equivalent 2 mol of H_2, increasing the reducing potential of Earth's surface (Kasting, 2013).

The net effect on Earth's redox budget is the same regardless of the locus of magnetite formation (reaction 1), but in contrast to thermochemical and diagenetic modes of magnetite formation (reactions 2 and 3), magnetite formed in the water column would be directly controlled by and thus record primary information on the chemistry and ecology of ancient seawater. Importantly, the formation of water column magnetite (reactions 4 and 5) would tend to inhibit microbial Fe(III) reduction (reaction 6), as Fe(III) sequestered in magnetite is poorly biologically reactive (Kostka and Nealson, 1995). At the same time, water column magnetite formation would tend to channel organic C from respiration to hydrogen production through fermentation (reaction 7). It would thus also implicate the processes responsible for magnetite formation in controlling the deposition of IFs, their mineralogy, oxidation state and

corresponding influences on Earth surface redox budgets. While low temperature magnetite precipitation in modern soils and sediments is frequently observed (Karlin et al., 1987), primary water column magnetite formation and its role in IF deposition and early Earth evolution is seldom considered.

Modern ferruginous environments provide natural laboratories to examine processes extensible to the Fe-rich Precambrian oceans (Crowe et al., 2008; Crowe et al., 2014b). To investigate Fe-cycling and mineral formation under ferruginous conditions we conducted experiments in, and collected samples from Lakes Matano and Towuti (herein referred to as LM and LT) on Sulawesi Island, Indonesia. LM and LT are part of the interconnected Malili Lakes system. The catchment basin surrounding the lakes is dominated by ultramafic rocks of ophiolitic origins and weathering of these rocks has led to development of exceptionally Fe-rich lateritic soils (Crowe et al., 2008; Russell et al., 2016). Heavy tropical rains deliver strong fluxes of Fe (oxyhydr)oxides from these soils to the lakes, which exert an overwhelming influence on the lakes' biogeochemistry (Crowe et al., 2008; Zegeye et al., 2012). Both LM and LT are physically and chemically stratified and characterized by persistently anoxic, Fe(II)-rich (~140 and ~10 μM respectively), and virtually sulfate free (< 5 μM) deep waters (Crowe et al., 2014b) (Fig. 1). We combined geochemical and mineralogical analyses to evaluate Fe cycling and pelagic Fe mineral formation in both LM and LT, revealing that water column Fe(III) reduction leads directly to the formation of primary authigenic magnetite. This magnetite takes conspicuous morphologies and comprises a major component of the primary Fe mineral assemblage exported to the underlying sediments.

2.0 Materials and methods

2.1 Sample Collection

Sediment trap sampling was performed in May and June 2015. Sediment traps consisting of four tubes (8 cm in diameter, 57 cm tall) were deployed at the specified depths in each lake (Fig. 1). These sediment traps were deployed for 6.2 and 3.0 days in LM and LT, respectively. During recovery, material recovered from half of the sediment traps retrieved from each depth (2 of 4 tubes) was immediately filtered onto glass-fiber filters (0.2 μm) using a peristaltic pump, with no exposure to the atmosphere. Filters were transferred directly to 15 ml falcon tubes

containing 5 ml 0.5 N HCl. The other half of the sediment was quantitatively transferred, again avoiding exposure to the atmosphere, into 12 ml Exetainers with no headspace.

Sediment and water samples were recovered from both lakes in years 2014 and 2015. Water temperature, oxygen concentration, chlorophyll *a*, light intensity, and transmissometry were determined in situ with a conductivity-temperature-depth probe (CTD; Sea-Bird, SBE-19; Sea-Bird Electronics, Bellevue, WA, USA). All water samples were collected with 5 L (Niskin; General Oceanics, Miami, FL, USA) bottles attached in series to a stainless-steel cable and a hand-operated winch. The bottles were placed at depth to an accuracy of ±1 m with the help of a commercial fish finder (Furuno, FCV 585; Furuno Electric Co., Nishinomiya, Japan). Several sediment cores (<0.5 m) were retrieved from both lakes using a gravity corer. Water column pH was determined by inserting the pH electrode (ThermoScientific, Orion) into a Winkler bottle free of air bubbles containing the water column sample. Sediment sampling took place at water depths of 200 m in both lakes. The sites in both lakes are overlain by anoxic and Fe(II)-rich (ferruginous) water. Short cores were sectioned in a N_2 flushed glove bag at a resolution of 0.5, 1, and 2 cm resolution for the upper 1, 1-10, and below 10 cm, respectively. We measured sediment porewater pH in the field by homogenizing 2 ml of sediment in 2 ml of deionized water and measuring this slurry after 2 min. A sub sample of 0.5 g of sediment from each interval was immediately extracted in 1 ml 0.5 N HCl (Lovley and Phillips, 1986b; Thamdrup et al., 1994), and Fe-speciation on these easily extractable phases was measured spectrophotmetrically on site using the ferrozine assay (Viollier et al., 2000). The residual sediment from each section was preserved in N_2 flushed falcon tubes and sealed in N_2 flushed aluminum foil bags.

Short-core sediment Fe-speciation measurements were performed on anaerobically preserved and freeze dried sediment samples following the method of (Poulton and Canfield, 2005). Sample masses of 100-200 mg of dry sediment were weighed into 15 ml centrifuge tubes, and the sequential extraction scheme was followed as indicated in (Poulton and Canfield, 2005), only substituting 0.5 M HCl in place of the hydroxylamine hydrochloride leach (Table 1). This was done so that both Fe(II) and Fe(III) could be determined in this reactive hydrous (oxyhydr)oxide fraction. The highly reactive, "Fe_{HR}" pool is defined as the sum of carbonate-associated Fe ($Fe_{Aca,}$ acetate), hydrous (oxyhydr)oxides including ferrihydrite and lepidocrocite ($Fe_{HCl,}$ 0.5 N HCl extractable Fe), ferric (oxyhydr)oxides including hematite and goethite ($Fe_{Dith,}$ dithionite extractable Fe), and magnetite ($Fe_{Oxa,}$ oxalate extractable Fe). The non reactive, "Fe_{NR}"

pool is defined as Fe contained in silicate minerals ($Fe_{Sil,}$ near boiling 6 N HCl extractable Fe after removal of reactive phases). Fe-speciation was also conducted on filtered sediment trap material by applying each extraction directly to the filter within the 15 ml centrifuge tube. All Fe concentration measurements were performed using a Flame Atomic Absorption Spectrophotometer (Flame AAS). Precision on triplicate measurements was <1% (2SD) and our limit of detection was ~0.1 μg g^{-1}. Our extractions dissolved >92% of the Fe from the PACS-2 international reference standard.

2.2 *Sample preparation*

We prepared magnetic separates from the sediments of LM and LT for multi-method spectroscopic analyses and to test the selectivity of the oxalate extraction. To accomplish this we treated a sub-set of sediment samples with dithionite, to remove reducible Fe (oxyhydr)oxide mineral phases (Poulton and Canfield, 2005) and make magnetite easier to visualize and image. We then carefully and as quantitatively as possible, separated magnetic grains from the residual sediment by hand using neodymium magnets. Sub-samples of both the magnetic extracts and residual magnetite-free sediment were taken and stored under N_2 for spectroscopic and geochemical analyses.

2.3 Fe flux calculations

To calculate water column Fe fluxes, area specific Fe sedimentation rates were determined by dividing the concentration of Fe captured by the sediment trap in each operationally defined mineral phase (mmol), by the area of the sediment trap (0.005 m^2) and the deployment time to yield Fe fluxes in units of mmol m^{-2} yr^{-1}. In the deposited sediments, area specific Fe accumulation rates were determined by multiplying volume specific Fe concentrations (mmol m^{-3}) by previously determined sedimentation rates (0.0008 and 0.00019 m yr^{-1} in LM and LT, respectively, Crowe et al. (2008); Russell et al. (2016); Russell et al. (2014)) to yield sediment Fe accumulation rates in mmol m^{-2} yr^{-1}. Deep-water diffusive Fe(II) gradients in each lake were determined by multiplying Fe(II) concentration gradients with diffusivity coefficients. Bottom water concentrations of Fe(II) in LM and LT are 0.140 and 0.010 mmol l^{-1}, respectively (Fig. 1), and these dissolved pools are quantitatively oxidized at the chemocline (Fig. 1), driving upward diffusive fluxes of Fe(II). We calculate Fe(II) gradients as 1.5 and 0.6

mM m^{-4} in LM and LT, respectively (Fig. 1). Upward diffusional Fe(II) fluxes were estimated by multiplying the Fe(II) gradients by the eddy diffusivity coefficient (0.1 and 0.6 m^2 d^{-1} in LM and LT respectively (Crowe et al., 2014a; Katsev et al., 2010)).

2.4 Saturation state calculations

Saturation indices were calculated for the relevant mineral species as:

$$SI = -log\frac{IAP}{K_{sp}} \quad (5)$$

where IAP is the ion activity product for the relevant mineral phase and K_{sp} is its corresponding solubility product. Saturation indices greater than 0 indicate that water is supersaturated with respect to the relevant mineral, whereas those less than 0 indicate that water is undersaturated with respect to a given mineral phase (Fig. 1d). Solubility products for all mineral phases were taken from the PHREEQC database (Parkhurst and Appelo, 1999). Mineral precipitation reactions and solubility products are tabulated in (Table 2). Water column dissolved inorganic carbon (DIC) concentrations were calculated based on charge balance using the concentration of all major ions in solution (Crowe et al., 2008; Zegeye et al., 2012). Activity coefficients (γ) for the major ions in solution (γ) were calculated with the Debye-Hückel equation (6), which relates γ to z and I;

$$log\gamma_i = -0.5z_i^2\sqrt{I} \quad (6)$$

As γ is a function of the ionic strength of the lake waters (I), we calculated this using equation (7);

$$I = \frac{1}{2}\Sigma\, m_i z_i^2 \quad (7)$$

where m_i and z_i are the molality and charge of each ion respectively. Water column dissolved Fe(III) concentrations in LM and LT were calculated assuming equilibrium (*SI* = 0) with either goethite or ferrihydrite as the solubility controlling phase.

2.5 SEM Microscopy

Anoxically preserved water column and sediment samples were preserved using a 1% osmium tetroxide solution buffered with 0.1 M PIPES at pH 6.8. Filters were rinsed gently with

MQ water and then dried using an ethanol dehydration series. The filters were critical-point-dried using a Samdri795 from Toosimis Research Corporation. Finally, the filters were attached to a 12.5 mm stub and coated with 5 nm of iridium to ensure conductivity. The filters were imaged on a Helios FIB-SEM (FEI, Helios NanoLab 650) equipped with field emission gun. Fe(III) oxyhydroxides were confirmed through energy-dispersive X-ray spectroscopy (EDS) and elemental compositions determined based on X-ray fluorescence at the relevant emission energies for Fe, C and O. Multiple points were measured for each surface found. To verify that the micro-chemical analyses of the SEM-EDS accurately differentiate magnetite from other Fe-oxide phases, we analyzed two pure Fe-mineral standards; magnetite (Fe_3O_4) and goethite (FeO(OH)). On each standard we collected over 10 distinct EDS spots and compiled their Fe:O stoichiometries (wt%). We then performed bootstrap resampling of the mean Fe:O compositions for these standard minerals. We also obtained EDS spectra on framboids collected in the water column and sediments of LM and LT (n = 17) and performed bootstrapped resampling of their mean Fe:O values.

2.6 Raman Spectroscopy

Magnetically separated grains from LM sediment (section 2.2 above) were mounted in epoxy, and polished using a micro-diamond paste. Raman spectroscopy was conducted using a Horiba Ltd. XploRa Plus μ-Raman spectrometer. Analyses were done using a green laser (λ = 532 nm), which provided a power at the sample surface of 2.5 mW and were done using a 100× objective focused down to a spot ~1 μm in diameter. Spectral slit width was set at 100 μm and the confocal hole was kept at 300 μm. Data were collected during three cycles of 30 s to optimize the full width at half-maximum of resolved Raman bands, while minimizing possible effects of heating or oxidation.

3.0 Results and Discussion

3.1 Fe-speciation

Canonically reactive Fe (Fe_{HR}; Table 1), which is thought to represent Fe-species reactive towards anaerobic microbial respiration and chemical reduction (Canfield et al., 1992), is the largest component (>90%) of the total Fe pool in suspended and deposited material from both

LM and LT (Fig. 2, Table 3 and Table 4). Analyses of water column particles collected from sediment traps deployed above and below each lake's chemocline, as well as their bottom sediments, reveal Fe mineral transformations that take place both during transport through the water column and during early sediment diagenesis in the uppermost deposited sediments. The speciation of Fe in sedimenting material from LM and LT is similar, and both shallow and deep sediment traps capture Fe that is mostly in the reactive, Fe_{HR}, form (Fig. 2 and Table 3). This Fe_{HR} is dominated by Fe_{Aca} (operationally defined as siderite), $Fe(III)_{HCl}$ (operationally defined as ferrihydrite) and Fe_{Dith} (operationally defined as goethite) extractable phases. In LM, these three pools together account for 83% and 70% of the total particulate Fe recovered in the shallow and deep traps, respectively, whereas in LT they account for 79% and 77% respectively (Fig 2, Table 3). These pools comprise Fe(III) mineral phases that are energetically favorable electron acceptors for anaerobic microbial respiration under standard-state conditions (Stumm and Morgan, 1988). The strong flux of Fe_{HR} thus provides an ample potential source of Fe(III), which through microbial respiration can be converted to, and accumulate as, Fe(II) under anoxic conditions.

The $Fe(III)_{HCl}$ pool, traditionally thought to represent the form most easily accessed for microbial respiration (Lovley and Phillips, 1986a), delivered to the lakes' anoxic waters is entirely reduced directly within the water column and is thus quantitatively converted to dissolved Fe(II) and Fe(II)-bearing minerals (Table 3, Fig. 2). Dissolved Fe(II) accumulates within the water column of both lakes. Equilibrium speciation calculations reveal that waters below the chemoclines in both LM and LT are supersaturated with respect to magnetite. Waters in LT are undersaturated with respect to siderite and carbonate green rust, while waters in LM are undersaturated with respect to green rust and moderately supersaturated with respect to siderite (Fig. 1d). Comparing the speciation of Fe captured in the upper sediment traps and Fe buried in the uppermost sediments reveals that reduction of a considerable fraction of the $Fe(III)_{HCl}$ pool takes place between theses sediment traps (Table 3). In LT, consumption of the $Fe(III)_{HCl}$ pool occurs entirely between the bottom sediment trap and the sediment water interface, and $Fe(III)_{HCl}$ is entirely absent from the underlying sediments. Due to this Fe(III) reduction the deep sediments of LM and LT thus receive a negligible $Fe(III)_{HCl}$. Reduction of Fe(III) in the water column is also commensurate with increases in the proportion of extractable Fe(II) bearing phases, Fe_{Oxa} and Fe_{Aca}, which in the deep traps increases by over 27% in LM and

372 44% in LT, relative to the upper sediment traps (Fig. 2, Table 3 and Table 4). The conclusions
373 drawn from these results, and in particular that $Fe(III)_{HCl}$ is converted to Fe_{Oxa} (Fig. 2), however,
374 hinge on the selectivity of the extractions and their ability to the target specific mineral phases,
375 as designed. Notably, the oxalate leach is known to dissolve non-magnetite phases in some
376 environments (Slotznick et al., 2018) and so we explore oxalate selectivity in LM and LT below.

377 The oxalate extraction is highly selective for Fe_{Oxa} (i.e., magnetite) in sediment trap
378 material and deposited sediments from LM and LT, and this gives us confidence in our ability to
379 identify and quantify Fe_{Oxa} (herein referred to as magnetite) in both sedimenting particulate
380 matter from the water column and deposited sediments. Geochemical and multi-method
381 spectroscopic analyses confirmed that magnetically separated grains are magnetite ($Fe_{Magnetic}$,
382 Fig. 2, Fig. 3). After physical separation of magnetite grains using a magnet, we also leached the
383 residual non-magnetic material ($Fe_{Non\ Magnetic}$, Fig. 2) with oxalate, recovering <0.1% (<0.8%
384 from deposited sediments) of the total Fe (Fe_{NMOE}, Fig. 2), or less than 1% of the total oxalate
385 extractable Fe. This demonstrates that more than 99% of the Fe extracted with oxalate comes
386 from magnetite and less than 1% from the non-selective extraction of other phases. We thus
387 conclude that, while operationally defined, the oxalate extraction applied here is highly selective
388 for magnetite and yields precise and quantitative information on its abundance in sediment trap
389 material and deposited sediments.

390

391 *3.2 Microscopy*

392 We also confirmed the presence of magnetite in the water columns and sediments of LM
393 and LT using electron microscopic techniques and these analyses revealed different forms of
394 magnetite that can be attributed to both authigenic and detrital origins. In the deep sediment
395 traps, for example, we observed magnetite framboids (Fig. 3), which are clearly authigenic (Fig.
396 4), as well as irregularly shaped partly weathered grains of likely detrital provenance (Fig. 5).
397 Framboids are one of magnetite's most enigmatic crystal forms and natural occurrences have
398 only been sporadically observed in ancient sedimentary rocks and meteorites (Itambi et al., 2010;
399 Kimura et al., 2013; Suk et al., 1990). Magnetite framboids also form in response to microbial
400 Fe(III) mineral reduction in laboratory experiments (J O'Loughlin et al., 2015). We note that
401 biogenic magnetite can take hollow spheroidal forms (Li et al., 2017), akin to the framboids of

magnetite observed in LM and LT. Magnetites with spherical morphologies are also characteristic of magnetite produced during modern coal combustion (Goldhaber et al., 2004), however, based on the sedimentation rates in LM and LT, framboidal magnetites recovered from the deeper sediment intervals are thousands of years old, conclusively ruling out an anthropogenic source. We did not observe framboidal magnetites in material recovered from upper sediment traps, but they were ubiquitous in deposited sediments from both LM and LT (Fig. 3, Fig. 4). Their lack from the upper sediment traps implies that they form under anoxic conditions, as the likely result of microbial Fe(III) reduction (Fig. 4). Many of the framboids appear to be hollow and detailed observations of framboid surfaces reveal that they are comprised of aggregates of nano-scale euhedral, octahedral crystals – a common crystal habit of magnetite (Fig. 3c, e, f). Micro-chemical analyses confirmed that these crystal aggregates had the 3:4 Fe:O stoichiometry diagnostic of magnetite (Fig. 3g,h and Fig. 6). Raman microspectroscopy yielded well-resolved reflections at wavenumbers (~310, ~450 - 490 and ~700 cm^{-1}), which correspond to the primary E_g, T_{2G} and A_{1G} vibrational modes that are diagnostic for magnetite (Shebanova and Lazor, 2003) (Fig. 3h). Although the mechanisms causing framboid formation remain largely unknown, pyrite of similar morphology is known to form at redox interfaces in other stratified water columns (Wilkin and Barnes, 1997; Wilkin et al., 1996). SEM-EDS analyses also reveal that at the 95% confidence interval, the composition of framboids from the Malili lakes and the magnetite mineral standard are statistically indistinguishable (p value = 0.786) (Fig. 6). Consistent with the scarcity of sulfur in the Malili lakes system, furthermore, we did not detect sulfur in any of our EDS analyses, further supporting a water column origin and ruling out diagenetic pyrite oxidation as a mechanism for magnetite framboid formation (Suk et al., 1990) in LM and LT. Collectively, our observations imply that magnetite formation, including framboids, is the result of $Fe(III)_{HCl}$ reduction, primarily in the water columns of LM and LT.

Framboidal magnetites recovered from the anoxic water column are smaller (<10 μm in diameter, Fig. 3) and their surface crystallites are more anhedral than their sedimentary counterparts (Fig. 3 and Fig. 4). Both the sediment and water column framboids have pristine euhedral octahedral crystals with well-defined faces at miller indices of 111, 110 (Fig. 3). The water column framboid surfaces also display triangular crystals, indicative of octahedra, which may be in early growth stages. The sedimentary population of magnetite in both lakes displays a

wide range of sizes (20-50 μm in diameter), and this range overlaps the size distribution of framboids and other spherical Fe mineral structures observed in Precambrian IFs (Lougheed and Mancuso, 1973) (Fig 4 and Fig. 5).

3.3 Magnetite formation, Fe(III) reduction, and Fe recycling

Comparisons of magnetite fluxes recorded in the water columns and sediments reveal that most authigenic magnetite in LM and LT forms in the water column, with little modification in the underlying sediments. Magnetite fluxes recorded in the lower sediment traps are 79% and 55% greater than in the upper sediment traps from LM and LT, respectively (Fig. 2 and Table 4). This demonstrates magnetite formation directly within the water column, at depths between the two sediment traps. In LT magnetite fluxes recorded in the upper sediments are also greater than in lower sediment traps (Fig 2, Table 4), and this indicates further magnetite formation, likely in the deep waters as well as within the very uppermost deposited sediments. Throughout the upper 45 cm of the LT sediments, however, the flux of magnetite is roughly constant (Fig. 2e) revealing a lack of net magnetite formation or dissolution and implying that the primary source of authigenic magnetite is the water column and that this magnetite is stable in the sediment. This implies that, while magnetite contains Fe(III), it is not further reduced in the sediment. In LM, we were unable to calculate sediment magnetite fluxes, as the lake's steep bathymetry effectively focuses detrital Fe (6 N HCl extractable lithogenic Fe phases, Fe_{Sil} see Table 3) to the deeper sediments, diluting authigenic Fe mineral phases. Our results thus reveal that water column magnetite formation is the principal source of authigenic magnetite to the underlying sediments in LT, and that once deposited magnetite is not subject to further Fe(III) reduction or other diagenetic modification.

Magnetite formation in LM and LT is associated with Fe(III) reduction in the water column and uppermost sediments and represents an important sink for the Fe(II) produced. Increases in the fluxes of magnetite below the chemoclines of LM and LT are commensurate with the conversion of $Fe(III)_{HR}$ to $Fe(II)_{HR,}$ which indicates Fe(III) reduction within this depth interval. Between the upper and lower sediment traps, magnetite formation accounts for 16% and 24% of this Fe reduction, respectively (Table 4). In LT, there is continued conversion of $Fe(III)_{HR}$ to $Fe(II)_{HR}$ in the anoxic waters between the lower sediment trap and uppermost sediments and magnetite formation accounts for 31% of this (Table 4). Pelagic magnetite

464 therefore represents a substantial sink for Fe(II) resulting from the reduction of $Fe(III)_{HR}$ species
465 directly in the water columns of LM and LT.

466 The $Fe(III)_{HCl}$ delivered to the upper sediment trap of LT is entirely converted to
467 magnetite and $Fe(II)_{Aca}$ in the water column and this implies that an appreciable fraction of the
468 $Fe(III)_{HCl}$ delivered to the lake is preserved as magnetite in the sediments. We note that while the
469 Fe_{Aca} fraction is canonically attributed to siderite, the deep waters of LT are modestly
470 undersaturated with respect to siderite, implying that the Fe_{Aca} fraction might represent other
471 highly reactive reduced Fe minerals, like poorly crystalline Fe(II)-bearing clays (Jaisi et al.,
472 2008). The flux of $Fe(III)_{HCl}$ delivered to the upper sediment trap is 73 mmol m^2 yr^{-1}, and this
473 compares with magnetite and $Fe(II)_{Aca}$ fluxes of 29 and 52 mmol m^2 yr^{-1} in the uppermost
474 sediments, respectively (Table 4). The absence of $Fe(III)_{HCl}$ in these uppermost sediments
475 demonstrates that it is quantitatively reduced in the water column and uppermost sediments, as
476 noted above. Fe_{Dith} fluxes are the same in the upper sediment trap and uppermost sediment
477 revealing a lack of conversion of $Fe(III)_{HCl}$ to $Fe(III)_{Dith}$. Mass balance thus requires that the
478 consumption of $Fe(III)_{HCl}$ in the water column is entirely tied to the production of magnetite
479 (36%) and Fe_{Aca} (64%). Given that 66% of Fe within stoichiometric magnetite is also Fe(III), this
480 indicates that 24% of the Fe(III) delivered to the upper sediment trap is ultimately preserved in
481 magnetite, revealing that water column magnetite formation exerts a primary control on the
482 redox state of the underlying ferruginous sediments in both lakes.

483 The accumulation of dissolved Fe(II) in the water columns of LM and LT implies Fe
484 recycling with potential to support Fe dependent microbial metabolisms. To constrain rates of
485 conversion of the $Fe(III)_{HCl}$ pool to Fe(II) and rates of recycling we compared diffusive Fe(II)
486 fluxes to the fluxes of $Fe(III)_{HCl}$ delivered to the upper sediment traps. In LT the diffusional flux
487 of Fe(II) is 130 mmol m^2 yr^{-1} which, when divided by the delivery flux of $Fe(III)_{HCl}$ (73 mmol
488 m^2 yr^{-1}) implies recycling of not more than 2 times. In LM the diffusional flux of Fe(II) is 55
489 mmol m^2 yr^{-1} which, when divided by the delivery flux of $Fe(III)_{HCl}$ (19 mmol m^2 yr^{-1}) implies
490 recycling of not more than 3 times. Since $Fe(III)_{HCl}$ is the primary source of dissolved Fe(II) and
491 much of this is converted to magnetite and Fe_{Aca} the limited recycling implies that Fe dependent
492 microbial metabolisms are ultimately restricted by both the delivery flux of $Fe(III)_{HCl}$ to the lake
493 and its conversion to secondary Fe(II) bearing phases, which are ultimately removed through
494 sedimentation and burial.

3.4 Implications

Our findings from LM and LT imply that pelagic magnetite formation can be an important mode of Fe delivery to ferruginous sediments and by extension suggest that magnetite derived from the Precambrian oceanic water column may have been a primary contributor to IF deposition. Magnetite formation in lakes LM and LT is linked to water column reduction of $Fe(III)_{HCl}$ as the likely source of Fe(II) in magnetite, and a similar process could thus be envisioned for magnetite formation in the Precambrian oceans. IF magnetite textures are clearly the result of secondary recrystallization and this obscures identification of primary mineral phases (Bekker et al., 2010). Elemental compositions (Sun and Li, 2017), however, strongly imply a primary seawater source for the relevant precursor phases. Furthermore, lateral continuity in IF magnetite layers imply widespread deposition of these precursor phases directly from the water column.

Formation of primary water column magnetite and its deposition in IFs would have been directly influenced by seawater chemistry. In LM and LT, magnetite forms under high degrees of supersaturation, at circumneutral pH, at <1 to 10s of μM Fe(II), and at mM concentrations of dissolved inorganic carbon (DIC) (Fig. 1 and Crowe et al. (2008)). Notably, these Fe(II) concentrations are far lower than those thought to be required to induce magnetite formation in laboratory experiments (J O'Loughlin et al., 2015; Lovley, 1991; Lovley et al., 1987). Conditions similar to LM and LT, however, could be expected to support primary magnetite formation in the Precambrian oceans and, indeed, such conditions are in line with current reconstructions of Archean and Proterozoic seawater chemistry (Halevy et al., 2017). Our observation of primary water column magnetite formation, even at modest Fe(II) and relatively high DIC concentrations in LM and LT thus reveals that the sedimentary flux of iron-bearing particles to the Precambrian seafloor likely contained an appreciable fraction of magnetite. In LM and LT these conditions also support the formation and deposition of an appreciable, though poorly defined Fe_{Aca} (canonically considered siderite) phase. Fe_{Aca} precipitation in modern anoxic environments and laboratory experiments typically requires high degrees of supersaturation (Bruno et al., 1992; Jimenez-Lopez and Romanek, 2004; Roh et al., 2003). Previous modelling of the Precambrian Fe cycle, however, suggests siderite may comprise an important fraction (up to 60%) of the

sedimentary Fe sink even under close to equilibrium conditions ($SI_{Siderite}$ ~1)(Halevy et al., 2017), similar to conditions observed in LM and LT. In addition to magnetite, therefore, other possible primary phases like siderite, green rust (Halevy et al., 2017; Zegeye et al., 2012) and greenalite (Tosca et al., 2016), may also have been important contributors to IFs.

Recognition of magnetite formation in the water columns of LM and LT informs models of the Precambrian Earth system. Phase relations based on the mineralogy of IFs have been used to place constraints on the possible role of different greenhouse gases in climate regulation at the time of IF deposition (Reinhard and Planavsky, 2011; Rosing et al., 2010). Some reconstructions suggest that the presence of magnetite in IFs reflects ocean conditions close to equilibrium with respect to magnetite stability fields, which thus implies pCO_2 concentrations not much greater than today (~400 ppm) (Rosing et al., 2010). Such low concentrations of greenhouse gases would thus preclude greenhouse warming as a means to stabilize planetary temperatures during the Precambrian Eons when the Sun's luminosity was weaker (Rosing et al., 2010). This observation, notably, contrasts with diagenetic models for IF magnetite, which allow for conditions far from equilibrium with the ocean-atmosphere system (Reinhard and Planavsky, 2011) and yield model estimates for atmospheric CO_2 concentrations up to 100 times present atmospheric levels (~40,000 ppm). Magnetite formation in LM and LT takes place in the water column and under pCO_2 of -2.5 to -1.9 (~3000 to 10,000 ppmv) and this magnetite remains diagenetically stable under such conditions. Our observations in LM and LT thus suggest that magnetite could have formed in Precambrian oceans in equilibrium with an atmosphere that contained pCO_2 much greater than today. Furthermore, the apparent stability of magnetite in LM and LT implies that it would have been preserved in IF sediments, irrespective of similarly high pCO_2. Combined with other greenhouse gases, a ~10,000 ppmv CO_2 atmosphere falls short of, but approaches, a composition that would support warming sufficient for a clement climate. We note, however, both that our observation of magnetite stability is on relatively short (~1000 yr) timescales, and that magnetite may form and remain stable under much higher pCO_2. These uncertainties should be worked out in follow-on research.

Our observation of pelagic magnetite formation supports the idea that the Fe isotopic composition of IF magnetite captures signatures of water column Fe drawdown in response to Fe(II) oxidation (Busigny et al., 2014; Rouxel et al., 2005). Such water column Fe drawdown leaves residual Fe(II) isotopically light, and minerals that sequester Fe(II) in such a concentration

gradient record this light signal (Beard et al., 2003; Johnson et al., 2008; Rouxel et al., 2005). Isotopically light magnetites were deposited in IFs from the Meso- to Neoarchean and have been variably interpreted to reflect either water column Fe(II) drawdown (Busigny et al., 2014; Planavsky et al., 2009; Rouxel et al., 2005) or sedimentary diagenetic Fe(III) reduction (Johnson et al., 2008). Our findings from LM and LT imply both that Fe reduction is mostly pelagic and that magnetites form from Fe(III) reduction in the water column. This suggests that Fe(II) drawdown in the water column of Precambrian oceans likely contributed to the Fe isotope composition of IFs. This could be further tested through Fe isotope studies in LM and LT.

The export of magnetite from the water columns of LM and LT sets the redox state of the underlying sediments and by extension implicates a role for coupled C and Fe cycling in setting Earth's surface redox budgets and the protracted oxidation of Earth's surface throughout the Precambrian Eons. Water column magnetite formation sequesters Fe(III) in a poorly biologically reactive form (reaction 5), inhibiting Fe(III) reduction (reaction 6), and channeling organic C into pathways that ultimately fuel H_2 and CH_4 production via both biological and photochemical reactions (ex., reaction 7) (Holland, 2002; Kasting, 2013; Ozaki et al., 2018). In LT, 23% of the $Fe(III)_{HCl}$ is converted to magnetite in association with microbial Fe(III) reduction. With global fluxes of up to 40 Tmol yr^{-1} reactive Fe to the Precambrian oceans (Thompson et al., 2019), and a similar fraction of conversion to magnetite, which is consistent with typical IF magnetite contents (Klein and Beukes, 1989), we estimate that based on the Fe:C:H_2 stoichiometry of 4:1:2 reactions (5 and 7), organic C channeled into fermentation and methanogenesis could fuel hydrogen fluxes of 4.6 Tmol yr^{-1}. This is nearly equivalent to twice the modern oxidant production through organic carbon burial in marine sediments (Holland, 2002). Key parameters that influence relevant Fe mineral formation like pH, DIC (linked to pCO_2 through the carbonate system), Fe(II) concentrations, and Fe(III) production and consumption rates, as well as likely rates of microbial metabolism would thus influence H_2 production rates and ultimately planetary oxidation rates.

In LM and LT, primary magnetites often form in conspicuous framboidal morphologies (Fig. 3 and Fig. 4), which can thus be used to identify such primary magnetites in the rock record. Hematite (Fe_2O_3), framboids of similar size and morphology have been observed in multiple Precambrian IFs (Ahn and Buseck, 1990; Ayres, 1972; Lougheed and Mancuso, 1973). Leading models of framboid formation rely on the ferromagnetic properties of the precursor Fe-

phases that control framboid aggregation (Wilkin and Barnes, 1997), and thus it is unlikely that the framboids observed in IFs were originally deposited as non-magnetic phases, such as hematite. These hematite framboids, instead, have been attributed to post depositional oxidation of precursor pyrite framboids with biogenic origins (Lougheed and Mancuso, 1973). The oxidation of pyrite to magnetite, however, is accompanied by a significant molar volume reduction of 60%, and thus the preservation of the framboid microstructure during oxidation is unlikely (Wilkin and Barnes, 1997). At the same time, appreciable pyrite formation is not expected in the Archean oceans due to low seawater sulfate concentrations (Crowe et al., 2014b; Fakhraee et al., 2018). We alternatively suggest that the framboidal hematite grains found in IFs were originally deposited as magnetite, and oxidized to hematite during subsequent diagenesis and or metamorphism. Such a provenance is supported by our observations from LM and LT. We also note that recrystallization of nano-magnetites to larger magnetite grains leads to textures commonly observed in IFs and in laboratory experiments even under low-grade pressure and temperature regimes (Li et al., 2013). There is thus ample evidence in support of the idea that magnetites in IFs represent the likely post deposition alteration products of primary nanoscale magnetite precipitates produced in response to pelagic microbial Fe respiration.

Beyond their likely contribution to terrestrial IFs, framboidal magnetites have also been observed in meteorites. Our finding that magnetite framboids form in LM and LT in association with microbial Fe(III) reduction and are preserved in their sediments, combined with observations of magnetite framboid formation as the result of microbial Fe reduction in lab experiments (J O'Loughlin et al., 2015), implies that magnetite framboids provide a relatively stable biomarker diagnostic of microbial Fe respiration. Meteorite magnetite framboids may thus be relicts of ancient extraterrestrial microbial Fe metabolisms. Ability to visually identify framboids and, as we show here, determine their mineralogy through Raman microspectroscopy, holds considerable promise for detecting such biosignatures from ancient ferruginous oceans on Earth, or remotely on Mars and other terrestrial planets.

4.0 Conclusions

We find that in ferruginous Lakes Matano (LM) and Towuti (LT) in Indonesia that magnetite forms directly in the water column. This magnetite is one of the major products of microbial Fe(III) respiration and comprises an appreciable fraction of Fe exported to the

underlying sediment, where it plays an important role in setting sediment redox state. These authigenic magnetites often take conspicuous framboidal forms, which given their links to microbial Fe(III) respiration may be diagnostic of this process and represent biosignatures. By analogy to LM and LT, we argue that similar processes in Precambrian ferruginous oceans would also have caused primary water column magnetite formation. We further argue that this water column magnetite formation would have contributed to the deposition of IF, and like in LM and LT, magnetite deposition would have controlled the redox state of IFs and thus also influenced the evolution of Earth's overall redox budget at this time. Observations that primary magnetite forms directly in ferruginous water columns has important implications for the interpretation of sedimentary mineralogical and isotopic features and for models of the Precambrian Earth system, including climate.

References

Ahn, J.H., Buseck, P.R., 1990. Hematite nanospheres of possible colloidal origin from a Precambrian banded iron formation. Science 250, 111-113.

Amor, M., Busigny, V., Durand-Dubief, M., Tharaud, M., Ona-Nguema, G., Gelabert, A., Alphandery, E., Menguy, N., Benedetti, M.F., Chebbi, I., Guyot, F., 2015. Chemical signature of magnetotactic bacteria. Proceedings of the National Academy of Sciences of the United States of America 112, 1699-1703.

Ayres, D., 1972. Genesis of iron-bearing minerals in banded iron formation mesobands in the Dales Gorge Member, Hamersley Group, Western Australia. Economic Geology 67, 1214-1233.

Beard, B.L., Johnson, C.M., Von Damm, K.L., Poulson, R.L., 2003. Iron isotope constraints on Fe cycling and mass balance in oxygenated Earth oceans. Geology 31, 629-632.

Bekker, A., Slack, J.F., Planavsky, N., Krapez, B., Hofmann, A., Konhauser, K.O., Rouxel, O.J., 2010. Iron Formation: The Sedimentary Product of a Complex Interplay among Mantle, Tectonic, Oceanic, and Biospheric Processes. Economic Geology 105, 467-508.

Berner, R.A., 2003. The long-term carbon cycle, fossil fuels and atmospheric composition. Nature 426, 323-326.

Beukes, N.J., Klein, C., 1990. Geochemistry and sedimentology of a facies transition—from microbanded to granular iron-formation—in the early Proterozoic Transvaal Supergroup, South Africa. Precambrian Research 47, 99-139.

Bruno, J., Wersin, P., Stumm, W., 1992. On the influence of carbonate in mineral dissolution: II. The solubility of FeCO3 (s) at 25 C and 1 atm total pressure. Geochimica Et Cosmochimica Acta 56, 1149-1155.

Busigny, V., Planavsky, N.J., Jézéquel, D., Crowe, S., Louvat, P., Moureau, J., Viollier, E., Lyons, T.W., 2014. Iron isotopes in an Archean ocean analogue. Geochimica et Cosmochimica Acta 133, 443-462.

Canfield, D.E., Raiswell, R., Bottrell, S., 1992. The reactivity of sedimentary iron minerals toward sulfide. American Journal of Science 292, 659-683.

Catling, D.C., Claire, M.W., 2005. How Earth's atmosphere evolved to an oxic state: A status report. Earth and Planetary Science Letters 237, 1-20.

Catling, D.C., Zahnle, K.J., McKay, C.P., 2001. Biogenic methane, hydrogen escape, and the irreversible oxidation of early Earth. Science 293, 839-843.

Claire, M.W., Catling, D.C., Zahnle, K.J., 2006. Biogeochemical modelling of the rise in atmospheric oxygen. Geobiology 4, 239-269.

Cornell, R.M., Schwertmann, U., 2003. The iron oxides: structure, properties, reactions, occurrences and uses. John Wiley & Sons.

Crowe, S.A., Maresca, J.A., Jones, C., Sturm, A., Henny, C., Fowle, D.A., Cox, R.P., Delong, E.F., Canfield, D.E., 2014a. Deep-water anoxygenic photosythesis in a ferruginous chemocline. Geobiology 12, 322-339.

Crowe, S.A., O'Neill, A.H., Katsev, S., Hehanussa, P., Haffner, G.D., Sundby, B., Mucci, A., Fowle, D.A., 2008. The biogeochemistry of tropical lakes: A case study from Lake Matano, Indonesia. Limnology and Oceanography 53, 319-331.

Crowe, S.A., Paris, G., Katsev, S., Jones, C., Kim, S.-T., Zerkle, A.L., Nomosatryo, S., Fowle, D.A., Adkins, J.F., Sessions, A.L., Farquhar, J., Canfield, D.E., 2014b. Sulfate was a trace constituent of Archean seawater. Science 346, 735-739.

690 Fakhraee, M., Crowe, S.A., Katsev, S., 2018. Sedimentary sulfur isotopes and Neoarchean ocean
691 oxygenation. Science Advances 4.
692 Goldhaber, M., Callender, T., Reynolds, R., 2004. The geochemical and magnetic record of coal-
693 combustion products in West Virginia reservoir sediments and soils. Geochemical Investigations
694 in Earth and Space Science: a Tribute to Issac R. Kaplan, 159-186.
695 Halama, M., Swanner, E.D., Konhauser, K.O., Kappler, A., 2016. Evaluation of siderite and
696 magnetite formation in BIFs by pressure-temperature experiments of Fe(III) minerals and
697 microbial biomass. Earth and Planetary Science Letters 450, 243-253.
698 Halevy, I., Alesker, M., Schuster, E.M., Popovitz-Biro, R., Feldman, Y., 2017. A key role for
699 green rust in the Precambrian oceans and the genesis of iron formations. Nature Geoscience 10,
700 135.
701 Holland, H.D., 1984. The chemical evolution of the atmosphere and oceans. Princeton University
702 Press.
703 Holland, H.D., 2002. Volcanic gases, black smokers, and the Great Oxidation Event. Geochimica
704 Et Cosmochimica Acta 66, 3811-3826.
705 Holland, H.D., 2006. The oxygenation of the atmosphere and oceans. Philosophical Transactions
706 of the Royal Society B-Biological Sciences 361, 903-915.
707 Itambi, A.C., von Dobeneck, T., Dekkers, M.J., Frederichs, T., 2010. Magnetic mineral
708 inventory of equatorial Atlantic Ocean marine sediments off Senegal-glacial and interglacial
709 contrast. Geophysical Journal International 183, 163-177.
710 J O'Loughlin, E., A Gorski, C., M Scherer, M., 2015. Effects of phosphate on secondary mineral
711 formation during the bioreduction of akaganeite (β-FeOOH): Green rust versus framboidal
712 magnetite. Current Inorganic Chemistry 5, 214-224.
713 Jaisi, D.P., Dong, H.L., Morton, J.P., 2008. Partitioning of Fe(II) in reduced nontronite (NAu-2)
714 to reactive sites: Reactivity in terms of Tc(VII) reduction. Clays and Clay Minerals 56, 175-189.
715 Jiao, Y.Y.Q., Kappler, A., Croal, L.R., Newman, D.K., 2005. Isolation and characterization of a
716 genetically tractable photo autotrophic Fe(II)-oxidizing bacterium, Rhodopseudomonas palustris
717 strain TIE-1. Applied and Environmental Microbiology 71, 4487-4496.
718 Jimenez-Lopez, C., Romanek, C.S., 2004. Precipitation kinetics and carbon isotope partitioning
719 of inorganic siderite at 25 degrees C and 1 atm. Geochimica Et Cosmochimica Acta 68, 557-571.
720 Johnson, C.M., Beard, B.L., Klein, C., Beukes, N.J., Roden, E.E., 2008. Iron isotopes constrain
721 biologic and abiologic processes in banded iron formation genesis. Geochimica Et
722 Cosmochimica Acta 72, 151-169.
723 Karlin, R., Lyle, M., Heath, G.R., 1987. Authigenic magnetite formation in suboxic marine
724 sediments. Nature 326, 490-493.
725 Kasting, J.F., 2013. What caused the rise of atmospheric O-2? Chemical Geology 362, 13-25.
726 Katsev, S., Crowe, S.A., Mucci, A., Sundby, B., Nomosatryo, S., Haffner, G.D., Fowle, D.A.,
727 2010. Mixing and its effects on biogeochemistry in the persistently stratified, deep, tropical Lake
728 Matano, Indonesia. Limnology and Oceanography 55, 763-776.
729 Kimura, Y., Sato, T., Nakamura, N., Nozawa, J., Nakamura, T., Tsukamoto, K., Yamamoto, K.,
730 2013. Vortex magnetic structure in framboidal magnetite reveals existence of water droplets in
731 an ancient asteroid. Nature Communications 4.
732 Klein, C., 2005. Some Precambrian banded iron-formations (BIFs) from around the world: Their
733 age, geologic setting, mineralogy, metamorphism, geochemistry, and origin. American
734 Mineralogist 90, 1473-1499.

735 Klein, C., Beukes, N.J., 1989. Geochemistry and sedimentology of a facies transition from
736 limestone to iron-formation deposition in the early Proterozoic Transvaal Supergroup, South
737 Africa. Economic Geology 84, 1733-1774.
738 Koeksoy, E., Sundman, A., Byrne, J.M., Lohmayer, R., Planer-Friedrich, B., Halevy, I.,
739 Konhauser, K.O., Kappler, A., 2019. Formation of green rust and elemental sulfur in an analogue
740 for oxygenated ferro-euxinic transition zones of Precambrian oceans. Geology 47, 211-214.
741 Konhauser, K.O., Newman, D.K., Kappler, A., 2005. The potential significance of microbial
742 Fe(III) reduction during deposition of Precambrian banded iron formations. Geobiology 3, 167-
743 177.
744 Kostka, J.E., Nealson, K.H., 1995. Dissolution and reduction of magnetite by bacteria.
745 Environmental Science & Technology 29, 2535-2540.
746 Li, Y.-L., Konhauser, K.O., Kappler, A., Hao, X.-L., 2013. Experimental low-grade alteration of
747 biogenic magnetite indicates microbial involvement in generation of banded iron formations.
748 Earth and Planetary Science Letters 361, 229-237.
749 Li, Y.L., Konhauser, K.O., Zhai, M.G., 2017. The formation of magnetite in the early Archean
750 oceans. Earth and Planetary Science Letters 466, 103-114.
751 Lougheed, M., Mancuso, J., 1973. Hematite framboids in the negaunee iron formation,
752 Michigan; evidence for their Biogenic Origin. Economic geology 68, 202-209.
753 Lovley, D.R., 1991. Magnetite formation during microbial dissimilatory iron reduction. Iron
754 Biominerals, 151-166.
755 Lovley, D.R., Phillips, E.J., 1986a. Availability of ferric iron for microbial reduction in bottom
756 sediments of the freshwater tidal Potomac River. Appl. Environ. Microbiol. 52, 751-757.
757 Lovley, D.R., Phillips, E.J.P., 1986b. Organic matter mineralization with reduction of ferric iron
758 in anaerobic sediments. Applied and Environmental Microbiology 51, 683-689.
759 Lovley, D.R., Stolz, J.F., Nord, G.L., Phillips, E.J.P., 1987. Anaerobic production of magnetite
760 by a dissimilatory iron-reducing microorganism. Nature 330, 252-254.
761 Ozaki, K., Tajika, E., Hong, P.K., Nakagawa, Y., Reinhard, C.T., 2018. Effects of primitive
762 photosynthesis on Earth's early climate system. Nature Geoscience 11, 55-59.
763 Parkhurst, D.L., Appelo, C., 1999. User's guide to PHREEQC (Version 2): A computer program
764 for speciation, batch-reaction, one-dimensional transport, and inverse geochemical calculations.
765 Water-resources investigations report 99, 312.
766 Planavsky, N., Rouxel, O., Bekker, A., Shapiro, R., Fralick, P., Knudsen, A., 2009. Iron-
767 oxidizing microbial ecosystems thrived in late Paleoproterozoic redox-stratified oceans. Earth
768 and Planetary Science Letters 286, 230-242.
769 Poulton, S.W., Canfield, D.E., 2005. Development of a sequential extraction procedure for iron:
770 implications for iron partitioning in continentally derived particulates. Chemical Geology 214,
771 209-221.
772 Reinhard, C.T., Planavsky, N.J., 2011. Mineralogical constraints on Precambrian p(CO2). Nature
773 474, E1-E2.
774 Roh, Y., Zhang, C.L., Vali, H., Lauf, R.J., Zhou, J., Phelps, T.J., 2003. Biogeochemical and
775 environmental factors in Fe biomineralization: Magnetite and siderite formation. Clays and Clay
776 Minerals 51, 83-95.
777 Rosing, M.T., Bird, D.K., Sleep, N.H., Bjerrum, C.J., 2010. No climate paradox under the faint
778 early Sun. Nature 464, 744-U117.
779 Rouxel, O.J., Bekker, A., Edwards, K.J., 2005. Iron isotope constraints on the Archean and
780 Paleoproterozoic ocean redox state. Science 307, 1088-1091.

Russell, J.M., Bijaksana, S., Vogel, H., Melles, M., Kallmeyer, J., Ariztegui, D., Crowe, S., Fajar, S., Hafidz, A., Haffner, D., Hasberg, A., Ivory, S., Kelly, C., King, J., Kirana, K., Morlock, M., Noren, A., O'Grady, R., Ordonez, L., Stevenson, J., von Rintelen, T., Vuillemin, A., Watkinson, I., Wattrus, N., Wicaksono, S., Wonik, T., Bauer, K., Deino, A., Friese, A., Henny, C., Imran, Marwoto, R., Ngkoimani, L., Nomosatryo, S., Safiuddin, L., Simister, R., Tamuntuan, G., 2016. The Towuti Drilling Project: paleoenvironments, biological evolution, and geomicrobiology of a tropical Pacific lake. Scientific Drilling 21, 29-40.

Russell, J.M., Vogel, H., Konecky, B.L., Bijaksana, S., Huang, Y., Melles, M., Wattrus, N., Costa, K., King, J.W., 2014. Glacial forcing of central Indonesian hydroclimate since 60,000 y BP. Proceedings of the National Academy of Sciences of the United States of America 111, 5100-5105.

Shebanova, O.N., Lazor, P., 2003. Raman spectroscopic study of magnetite (FeFe2O4): a new assignment for the vibrational spectrum. Journal of Solid State Chemistry 174, 424-430.

Slotznick, S.P., Swanson-Hysell, N.L., Sperling, E.A., 2018. Oxygenated Mesoproterozoic lake revealed through magnetic mineralogy. Proceedings of the National Academy of Sciences 115, 12938-12943.

Stumm, W., Morgan, J.J., 1988. Aquatic chemistry; an introduction emphasizing chemical equilibria in natural waters. Current Contents/Agriculture Biology & Environmental Sciences, 18-18.

Suk, D., Peacor, D.R., Vandervoo, R., 1990. Replacement of pyrite framboids by magnetite in limestone and implications for palaeomagnetism. Nature 345, 611-613.

Sun, S., Li, Y.-L., 2017. Microstructures, crystallography and geochemistry of magnetite in 2500 to 2200 million-year-old banded iron formations from South Africa, Western Australia and North China. Precambrian Research 298, 292-305.

Thamdrup, B., Fossing, H., Jorgensen, B.B., 1994. Manganese, iron and sulfur cycling in a coastal marine sediment, Aarhus Bay, Denmark. Geochimica Et Cosmochimica Acta 58, 5115-5129.

Thompson, K.J., Kenward, P.A., Bauer, K.W., Warchola, T., Gauger, T., Martinez, R., Simister, R.L., Michiels, C.C., Llirós, M., Reinhard, C.T., Kappler, A., Konhauser, K.O., Crowe, S.A., 2019. Photoferrotrophy, deposition of banded iron formations, and methane production in Archean oceans. Science Advances 5.

Tosca, N.J., Guggenheim, S., Pufahl, P.K., 2016. An authigenic origin for Precambrian greenalite: Implications for iron formation and the chemistry of ancient seawater. Geological Society of America Bulletin 128, 511-530.

Viollier, E., Inglett, P.W., Hunter, K., Roychoudhury, A.N., Van Cappellen, P., 2000. The ferrozine method revisited: Fe(II)/Fe(III) determination in natural waters. Applied Geochemistry 15, 785-790.

Vuillemin, A., Wirth, R., Kemnitz, H., Schleicher, A.M., Friese, A., Bauer, K.W., Simister, R., Nomosatryo, S., Ordoñez, L., Ariztegui, D., 2019. Formation of diagenetic siderite in modern ferruginous sediments. Geology 47, 540-544.

Walker, J.C.G., 1984. Suboxic diagenesis in banded iron formations. Nature 309, 340-342.

Wilkin, R.T., Barnes, H.L., 1997. Formation processes of framboidal pyrite. Geochimica Et Cosmochimica Acta 61, 323-339.

Wilkin, R.T., Barnes, H.L., Brantley, S.L., 1996. The size distribution of framboidal pyrite in modern sediments: An indicator of redox conditions. Geochimica Et Cosmochimica Acta 60, 3897-3912.

Zegeye, A., Bonneville, S., Benning, L.G., Sturm, A., Fowle, D.A., Jones, C., Canfield, D.E., Ruby, C., MacLean, L.C., Nomosatryo, S., Crowe, S.A., Poulton, S.W., 2012. Green rust formation controls nutrient availability in a ferruginous water column. Geology 40, 599-602.
Zerkle, A.L., Claire, M., Domagal-Goldman, S.D., Farquhar, J., Poulton, S.W., 2012. A bistable organic-rich atmosphere on the Neoarchaean Earth. Nature Geoscience 5, 359-363.

Acknowledgments

This work was funded through NSERC Discovery Grants to Sean A. Crowe (0487) and Roger Francois, the Canadian Foundation for Innovation, the Canada Research Chairs Program, and a UBC 4-Year Fellowship and a GFZ Expedition grant to Jens Kallmeyer, and SNSF grant to A. Vuillemin (P2GEP2 148621). Gethin Gowen assisted with the SEM imaging. Rhy McMillan helped with the preparation of samples for Raman microspectroscopy and Jan Axel Kitte aided in the fieldwork. This research was carried out with permission from the Ministry of Research, Technology, and Higher Education of the Republic of Indonesia (Ritekdikti, RISTEK), the Natural Resources Conservation Center (BKSDA), and The government of Luwu Timur of Sulawesi, Indonesia. The Director of Research Center for Limnology (RCL) - Indonesian Institute of Sciences (LIPI), Tri Widiyanto (RCL-LIPI), Aan Diyanto (RCL-LIPI) and staff of RCL-LIPI all contributed to the logistics of sampling in Indonesia.

The authors declare no conflict of interest.

Data and materials availability: The datasets and models generated during and/or analyzed during the current study are available from the corresponding author on reasonable request.

Figures and Tables

Table 1. Description of Fe speciation extractions. Reactive Fe (Fe_{HR}) refers to the sum of Fe_{Aca}, $Fe(II)_{HCl}$, $Fe(III)_{HCl}$, Fe_{Dith}, and Fe_{Oxa} pools. Unreactive Fe (Fe_{NR}, Main Text) refers to the Fe_{Sil} pool.

Operationally defined Fe – mineral phases	Extractant
Siderite, Fe_{Aca}	1 M Na-acetate pH 4.5, 24 h (Poulton and Canfield, 2005)
Lepidocrocite, Ferrihydrite, Fe(II) and $Fe(III)_{HCl}$	0.5 M HCl, 1 h (Thamdrup et al., 1994)
Goethite, Hematite, Fe_{Dith}	0.35 M acetic acid/0.2 M Na-citrate Na-dithionite, 2 h (Poulton and Canfield, 2005)
Magnetite, Fe_{Oxa}	0.2 M ammonium oxalate/0.17 M oxalic acid, 6 h (Poulton and Canfield, 2005)
Silicate Fe, Fe_{Sil}	Near boiling 6 M HCl, 24 h (Poulton and Canfield, 2005)

879 **Table 2. Mineral reactions used to calculate saturation indices in Figure. 1.**

Mineral Reaction	K_{sp}	Database
Magnetite $Fe_3O_4 + 8H^+ = 2Fe^{+3} + Fe^{+2} + 4H_2O$	2.53E+03	PHREEQC
Siderite $FeCO_3 = Fe^{+2} + CO_3^{-2}$	5.75E-11	PHREEQC
Goethite $FeOOH + 3H^+ = Fe^{+3} + 2H_2O$	3.10E+00	PHREEQC
Ferrihydrite $Fe(OH)_3 + 3H^+ = Fe^{+3} + 3H_2O$	1.55E+03	PHREEQC
Carbonate Green Rust $Fe_6(OH)12CO_3 + 13H^+ = 4Fe^{2+} + 2Fe^{3+} + HCO_3^- + 12H_2O$	1.26E+39	PHREEQC

880
881
882
883
884
885
886
887
888
889
890
891
892
893
894
895
896
897
898

899 **Table 3. Water column Fe-speciation results.**

	Towuti (LT) 2015	Towuti (LT) 2015
	110 m	160 m
Phase	**% of Fe_{Tot}**	**% of Fe_{Tot}**
Fe_{NR}	10	6
Fe_{HR}	90	94
$Fe_{(II)}$	14	18
$Fe_{(III)}$	77	77
Fe_{Aca}	7	5
$Fe(II)_{HCl}$	4	11
$Fe(III)_{HCl}$	39	32
Fe_{Dith}	33	41
$Fe_{Oxa(II)}$	2	2
$Fe_{Oxa(III)}$	5	4
$Fe_{Non\ Magnetic}$	94	74
$Fe_{Magnetic}$	6	25
$Fe_{Non\ Magnetic\ Oxalate\ Extractable}$	0.5	1
Total Fe (µg)	436	740
	Matano (LM)	**Matano (LM)**
	90 m	**130 m**
Phase	**% of Fe_{Tot}**	**% of Fe_{Tot}**
Fe_{NR}	7	6
Fe_{HR}	93	94
$Fe_{(II)}$	29	41
$Fe_{(III)}$	64	53
Fe_{Aca}	24	23
$Fe(II)_{HCl}$	1	15
$Fe(III)_{HCl}$	17	8
Fe_{Dith}	41	39
$Fe_{Oxa(II)}$	3	3
$Fe_{Oxa(III)}$	6	6
$Fe_{NonMagnetic}$	99	96
$Fe_{Magnetic}$	0	4
$Fe_{NonMagnetic\ Oxalate\ Extractable}$	1	1
Total Fe (µg)	525	948

900

901

902 **Table 4. Fe fluxes in the Malili lakes.**

903

Sediment Trap Samples	Magnetite Flux (mmol m^{-2} yr^{-1})	Fe_{Aca} Flux (mmol m^{-2} yr^{-1})	$Fe(III)_{HCl}$ (mmol m^{-2} yr^{-1})	Total $Fe_{HR}(II)$ Flux (mmol m^{-2} yr^{-1})	Total $Fe_{HR}(III)$ Flux (mmol m^{-2} yr^{-1})	Magnetite Production (mmol m^{-2} yr^{-1})	Fe(III) Reduction (mmol m^{-2} yr^{-1})
Matano, 90 m	11	13	19	32	73	8	52
Matano, 130 m	19	15	16	84	107		
Towuti, 110 m	13	28	73	26	145	7	30
Towuti, 160 m	20	47	101	56	245		
Sediment Samples							
Matano Core Top (0.25 cm)	ND	ND	ND	ND	ND	ND	ND
Matano Core Bottom (20 cm)	ND	ND	ND	ND	ND		
Towuti Core Top (0.25 cm)	29	52	0	84	89	0	31
Towuti Core Bottom (40 cm)	27	57	0	114	51		

Figure 1. Chemical and physical properties of LT (top panels) and LM (bottom panels). The blue hexagons on the y-axes represent the sediment trap deployment depths in LT and LM, 110 and 160 m and 90 and 130 m respectively. **a)** Dissolved O_2 and Fe(II). **b)** Light transmission. **c)** pH. **d)** Mineral saturation indices. Closed black circles represent the SI for magnetite calculated using Fe(III) concentrations assuming ferrihydrite saturation (Mg_F). Open black circles represent the SI for magnetite calculated using Fe(III) concentrations assuming goethite saturation (Mg_G). We note both lakes' deep waters are oversaturated with respect to magnetite. Closed brown circles represent the SI for siderite (Sid). Closed green circles represent the SI for carbonate green rust (GR). See Table 2 for minerals reactions and solubility products.

Figure 2. Malili lake Fe-speciation and magnetite fluxes. a-d) Water column Fe-speciation plots. Each operationally defined Fe-phase is normalized to the total Fe content of the sample. $Fe_{Magnetic}$, $Fe_{Non\ Magnetic}$ and Fe_{NMOE}, refers to our sediment mass balance oxalate leaching tests. **e)** Photographs of filtered sediment trap material from LM. We note the striking color difference of material sedimenting above (shallow sediment trap, 90 m) and below (deep sediment trap, 130 m) the chemocline. **f)** Magnetite fluxes in the sediment traps and sediments in LM and LT. LT core top samples come from the 0 – 0.5 cm sediment depth interval, whereas core bottom samples from the 35 – 40 cm sediment depth interval.

Figure 3. Authigenic magnetite morphologies in the Malili lakes. a) Water column magnetite framboid captured in the LM deep sediment trap. Orange arrow indicates EDS spot location and corresponds to orange spectra in (g). **b)** Water column magnetite framboid captured in the LT deep sediment trap. **c)** A close up image of the framboid surface from (a). **d)** Magnetite framboid preserved in the LM sediment. Green arrow indicates EDS spot location and corresponds to green spectra in (g). **e)** A close up image of the framboid surface from (b), displaying immature magnetite octahedra. **f)** A close up image of the framboid surface from (a), displaying well-formed euhedral magnetite octahedra with identifiable crystal faces (111). **g)** SEM-EDS spectra of the framboids from (a) and (d). The orange and green arrows demarcate the EDS spot locations and corresponding spectral curves with the same colors from (a) and (d) respectively. Both framboids have Fe:O stoichiometry diagnostic of magnetite (see Fig. 6). **h)** Raman

spectrum of sediment framboids from LM. Solid spectra correspond to 4 different framboids. Grey triangles on the x-axis correspond to prominent spectral bands for magnetite (Cornell and Schwertmann, 2003; Shebanova and Lazor, 2003). We observe diagnostic magnetite peaks at wave numbers ~306, ~450 - 490, ~538 and ~668 (cm^{-1})(Shebanova and Lazor, 2003), with second order scattering between 1200 – 1400 cm^{-1}. **i)** A close up image of the framboid surface from (c), displaying nanoscale octahedral magnetite crystals.

Figure 4. Framboidal forms of magnetite in LM and LT sediment. We note that many of the framboids appear to be hollow.

Figure 5. Detrital magnetite morphologies in the LM and LT sediment. a) Octahedral crystal with pervasive dissolution pits. **b**) Rounded subhedral crystals with pervasive dissolution pits, grooves and surface etchings. **c**) Rounded euhedral octahedral crystal (dodecahedral face (211)) with surface etchings. **d**) Euhedral octaherdral crystal with surface etchings. **e**) Cracked and broken euhedral crystal with pervasive surface dissolution pits. **f**) Rounded euhedral octahedral crystal with truncations and surface etchings.

Figure 6. SEM-EDS statistical results. Plotted are histograms of the bootstrap resampled mean values of Fe:O compositions (n = 10), for the pure mineral standards compared to the combined water column and sediment magnetite framboid composition.

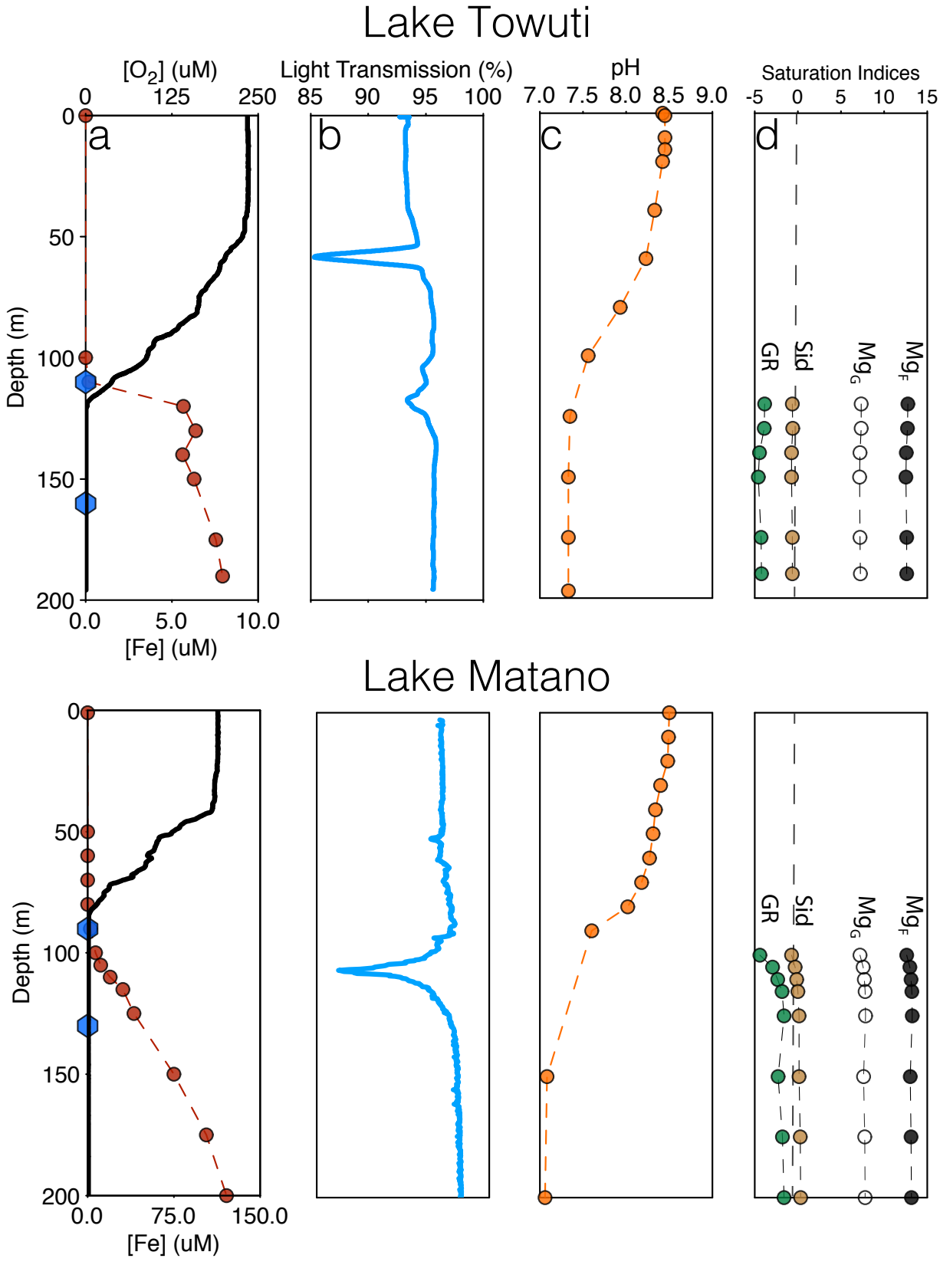
Lake Towuti
[O2] (uM)
Light Transmission (%)
pH
Saturation Indices
a
b
c
d
Depth (m)
[Fe] (uM)
GR
Sid
MgG
MgF
Lake Matano
Depth (m)
[Fe] (uM)
GR
Sid
MgG
MgF

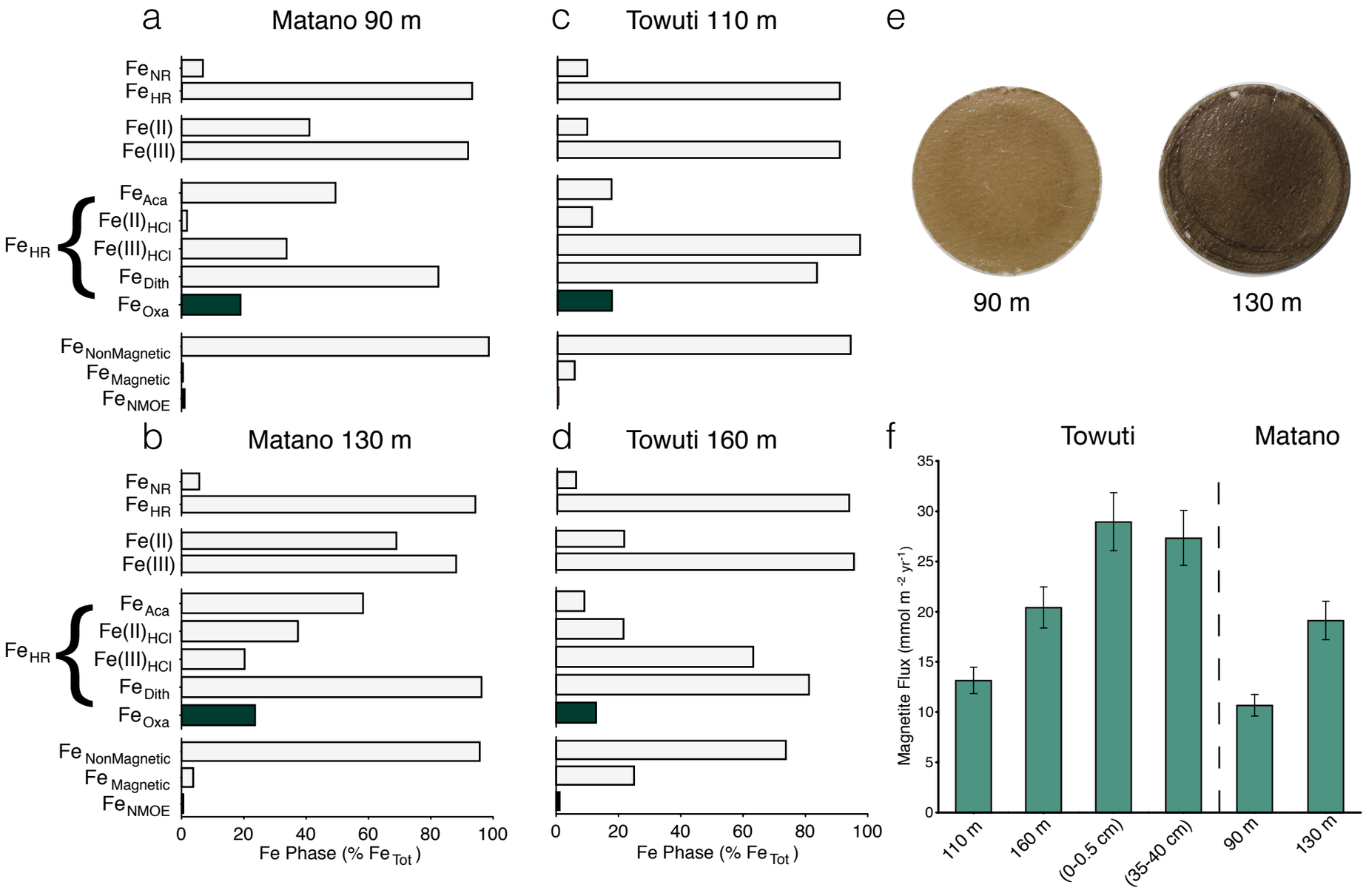
a
Matano 90 m
c
Towuti 110 m
e
Fe_{NR}
Fe_{HR}
Fe(II)
Fe(III)
Fe_{HR}
Fe_{Aca}
$Fe(II)_{HCl}$
$Fe(III)_{HCl}$
Fe_{Dith}
Fe_{Oxa}
$Fe_{NonMagnetic}$
$Fe_{Magnetic}$
Fe_{NMOE}
90 m
130 m
b
Matano 130 m
d
Towuti 160 m
f
Towuti
Matano
Magnetite Flux (mmol m $^{-2}$ yr^{-1})
0
5
10
15
20
25
30
35
110 m
160 m
(0-0.5 cm)
(35-40 cm)
90 m
130 m
0
20
40
60
80
100
Fe Phase (% Fe_{Tot})

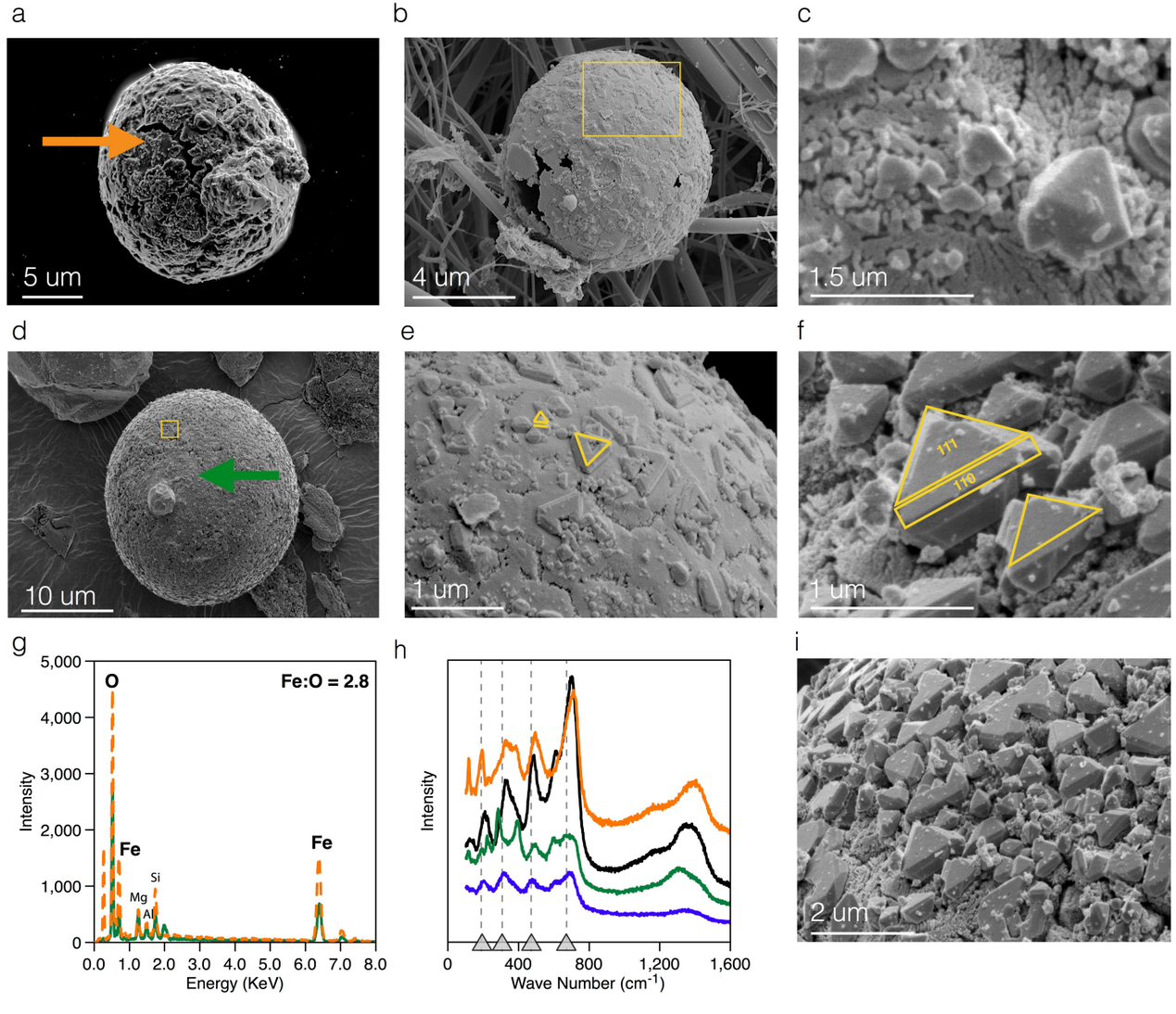
a
5 um
b
4 um
c
1.5 um
d
10 um
e
1 um
f
111
110
1 um
g
O
Fe:O = 2.8
Fe
Fe
Si
Mg
Al
Intensity
5,000
4,000
3,000
2,000
1,000
0
0.0 1.0 2.0 3.0 4.0 5.0 6.0 7.0 8.0
Energy (KeV)
h
Intensity
0
400
800
1,200
1,600
Wave Number (cm-1)
i
2 um

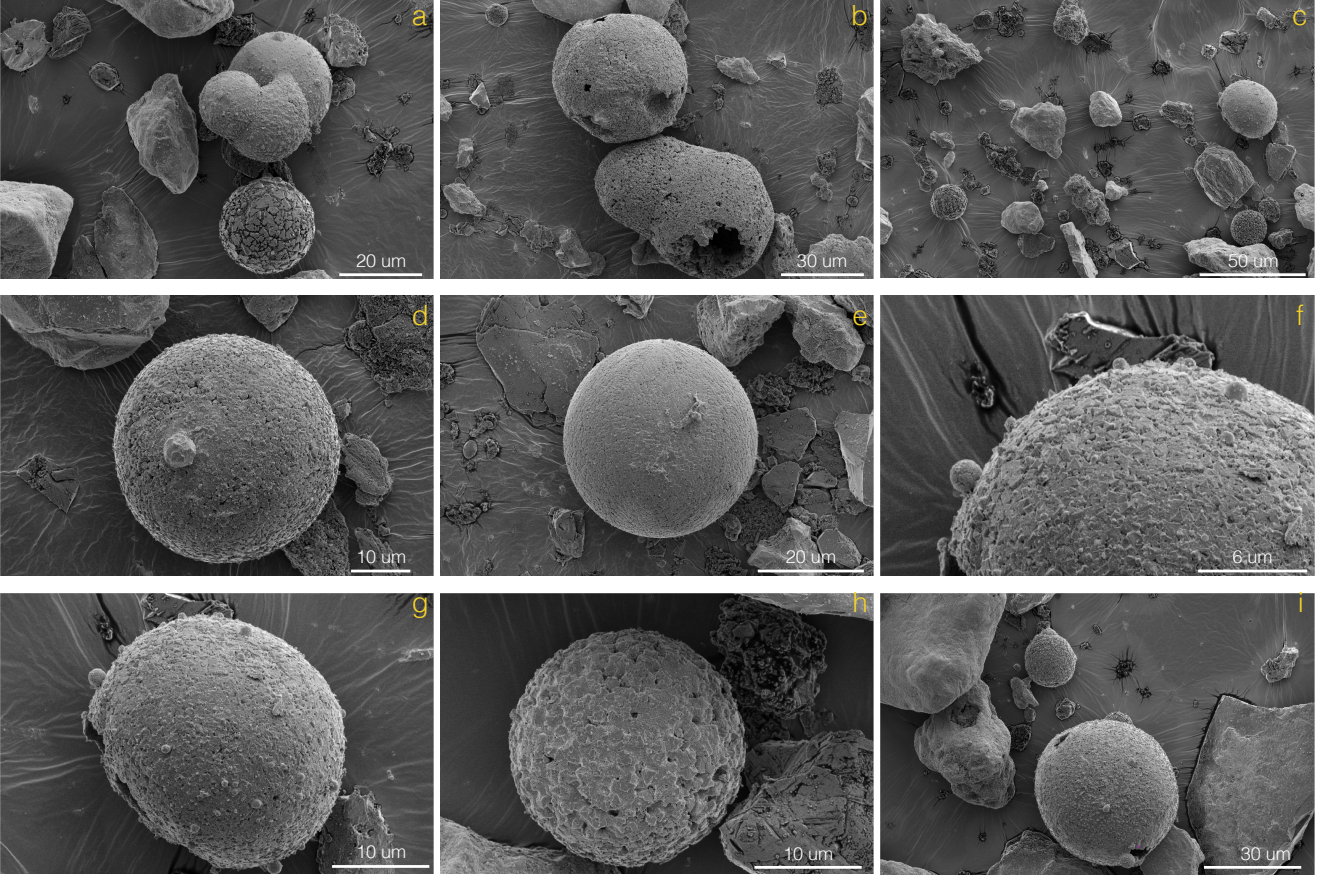
a
20 um
b
30 um
c
50 um
d
10 um
e
20 um
f
6 um
g
10 um
h
10 um
i
30 um

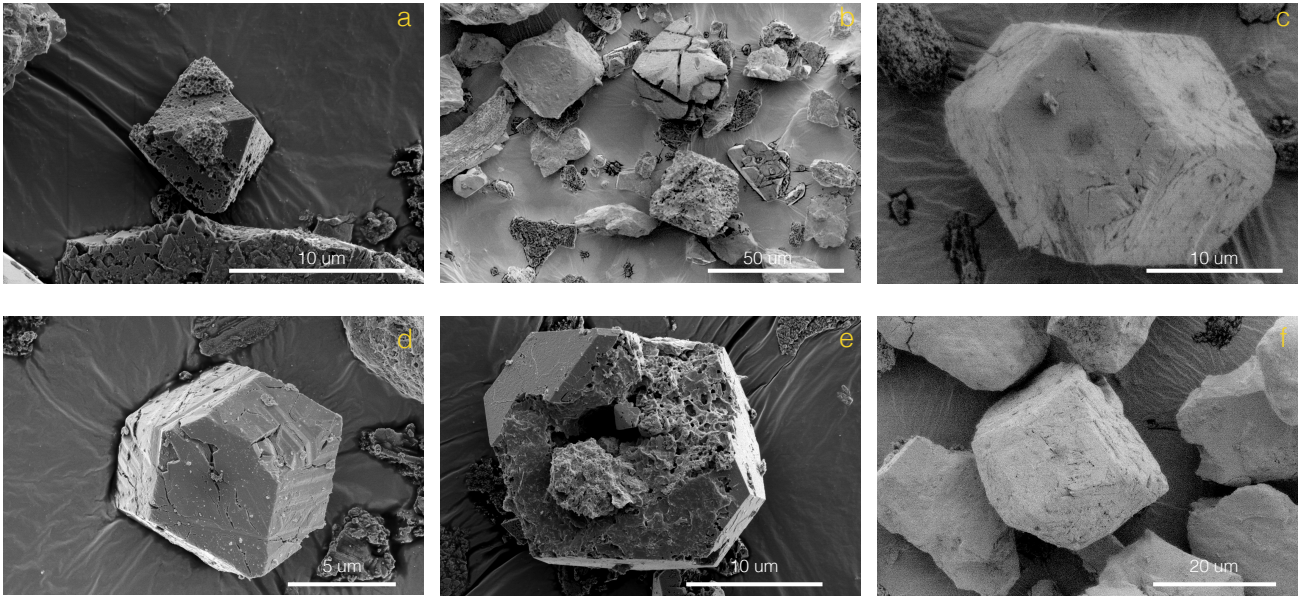
a
10 um
b
50 um
c
10 um
d
5 um
e
10 um
f
20 um

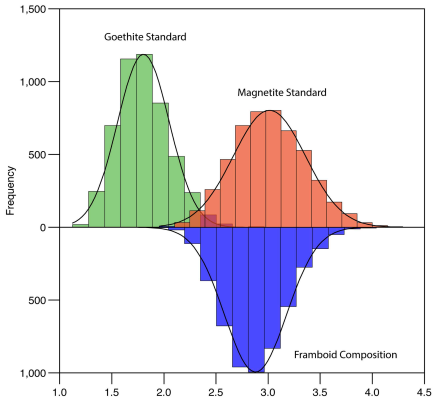
Goethite Standard
Magnetite Standard
Framboid Composition
Frequency
1,500
1,000
500
0
500
1,000
1.0
1.5
2.0
2.5
3.0
3.5
4.0
4.5
Fe:O Range